An 8.56 keV Absorption Line in the Hyperluminous X-Ray Source in NGC 4045: Ultrafast Outflow or Cyclotron Line?

Murray Brightman[1] ⓘ, Peter Kosec[2], Felix Fürst[3] ⓘ, Hannah Earnshaw[1] ⓘ, Marianne Heida[4] ⓘ, Matthew J Middleton[5] ⓘ,
Daniel Stern[6] ⓘ, and Dominic J Walton[7] ⓘ

[1] Cahill Center for Astrophysics, California Institute of Technology, 1216 East California Boulevard, Pasadena, CA 91125, USA; murray@srl.caltech.edu
[2] MIT Kavli Institute for Astrophysics and Space Research, Cambridge, MA 02139, USA
[3] Quasar Science Resources SL for ESA, European Space Astronomy Centre (ESAC), Science Operations Department, E-28692 Villanueva de la Cañada, Madrid, Spain
[4] European Southern Observatory, Garching, Germany
[5] Department of Physics & Astronomy, University of Southampton, Southampton, SO17 1BJ, UK
[6] Jet Propulsion Laboratory, California Institute of Technology, Pasadena, CA 91109, USA
[7] Centre for Astrophysics Research, University of Hertfordshire, College Lane, Hatfield AL10 9AB, UK
Received 2022 January 14; revised 2022 March 8; accepted 2022 March 14; published 2022 April 21

Abstract

We report on the discovery of an absorption line at $E = 8.56^{+0.05}_{-0.11}$ keV detected with a significance of $>3.3\sigma$ in the NuSTAR and XMM-Newton spectra of a newly discovered hyperluminous X-ray source ($L_X > 10^{41}$ erg s^{-1}) in the galaxy NGC 4045 at a distance of 32 Mpc. The source was first discovered serendipitously in a Swift/XRT observation of the galaxy, and Swift monitoring reveals a highly variable source changing by over an order of magnitude from maximum to minimum. The origin of the absorption line appears likely to be from highly ionized iron with a blueshift of 0.19c, indicating an ultrafast outflow. However, the large equivalent width of the line (EW $= -0.22^{+0.08}_{-0.09}$ keV) paired with the lack of other absorption lines detected is difficult to reconcile with models. An alternative explanation is that the line is due to a cyclotron resonance scattering feature produced by the interaction of X-ray photons with the powerful magnetic field of a neutron star.

Unified Astronomy Thesaurus concepts: Ultraluminous x-ray sources (2164); X-ray sources (1822); X-ray transient sources (1852); Neutron stars (1108); Black holes (162)

1. Introduction

Ultraluminous X-ray sources (ULXs) are X-ray sources located outside the nucleus of galaxies with observed fluxes that imply isotropic luminosities greater than 10^{39} erg s^{-1}. This luminosity is equivalent to the Eddington luminosity of a 10 $M_\odot$ black hole, the typical mass of known stellar-remnant black holes in our Galaxy. Hence, ULXs are either shining at super-Eddington rates, or the mass of the compact object is greater than 10 $M_\odot$. They are therefore of interest for studies of extreme accretion and black hole demographics.

Hyperluminous X-ray sources (HLXs) constitute the extreme end of the ULX luminosity function, with luminosities greater than 10^{41} erg s^{-1}, and are rare, with only 71 out of 1843 (4%) ULX candidates listed in the latest ULX catalog of Walton et al. (2022) reaching this luminosity. Their luminosities would seem to imply a black hole mass of >1000 $M_\odot$, an intermediate-mass black hole (IMBH), or a 10 $M_\odot$ black hole shining at 100 times Eddington. ESO 243-49 HLX-1 (Farrell et al. 2009) is a well-known HLX thought to be powered by an IMBH; however, another HLX, NGC 5907 ULX1 is known to be powered by a neutron star due to the detection of X-ray pulsations (Israel et al. 2017a). With a mass of only 1–2 $M_\odot$, the implied luminosity is ∼500 times its Eddington luminosity. Several other ULX pulsars are also known, including M82 X-2 (Bachetti et al. 2014), NGC 5907 ULX (Israel et al. 2017a), NGC 7793 P13 (Fürst et al. 2017; Israel et al. 2017b), NGC 300 ULX

(Carpano et al. 2018), NGC 1313 X-2 (Sathyaprakash et al. 2019), and M51 ULX7 (Rodríguez Castillo et al. 2020).

At such high apparent super-Eddington luminosities, powerful radiation-driven winds are expected from ULXs (Shakura & Sunyaev 1973; Poutanen et al. 2007). While no signatures for these outflows have been detected in any HLX source to date, likely due to their small numbers, such outflows have been detected in a number of ULXs, such as NGC 1313 X-1, NGC 5408 X-1, and NGC 6946 X-1 (Pinto et al. 2016, 2020). These have mostly been detected with the reflection grating spectrometer (RGS) instrument on XMM-Newton, e.g., NGC 55 ULX (Pinto et al. 2017), NGC 5204 X-1 (Kosec et al. 2018a), and NGC 300 ULX1 (Kosec et al. 2018b). Evidence for these was first seen in XMM-Newton/pn data as soft X-ray residuals (Middleton et al. 2014). Walton et al. (2016) also found evidence for the outflow from NGC 1313 X-1 in XMM-Newton/pn and NuSTAR data at 8.77 keV, and Kosec et al. (2018b) found evidence for the outflow from NGC 300 ULX1 in XMM-Newton/pn data.

In addition to these atomic absorption lines in ULX spectra, Brightman et al. (2018) reported the detection of a strong absorption line at 4.5 keV in the Chandra/ACIS spectrum of ULX8 in M51. Because the energy of this line was not consistent with atomic absorption, the authors concluded that it was due to a cyclotron resonance scattering feature (CRSF) produced by the interaction of X-ray photons with a powerful magnetic field (Gnedin & Sunyaev 1974; Truemper et al. 1978). This naturally identified the accretor as a neutron star, because black holes cannot produce such strong magnetic fields. Walton et al. (2018a) also identified a potential CRSF at 13 keV in the pulsed NuSTAR spectrum of NGC 300 ULX1.

Therefore, detecting and studying absorption features in the X-ray spectra of ULXs can reveal important information about the compact object powering the source and the extreme accretion onto it.

Here we report the discovery of a new HLX candidate in NGC 4045 with Swift/XRT and subsequent observations with Chandra, NuSTAR, and XMM-Newton. NGC 4045 is a spiral galaxy at a distance of 32.1 Mpc as determined from the Tully–Fisher relation (Tully et al. 2016) with a redshift of $z = 0.00659$ and hosts an optically identified active galactic nucleus (AGN) (Gavazzi et al. 2011). The galaxy also hosted the Type II supernova SN 1985B (Kosai et al. 1985). Uncertainties are given at the 90% confidence level unless otherwise stated.

2. X-Ray Data Analysis

2.1. Swift

We have been searching for new X-ray sources in observations made by NASA's Neil Gehrels Swift Observatory (Gehrels et al. 2004), specifically using its X-ray Telescope (XRT, Burrows et al. 2005). This search has already uncovered an X-ray-luminous tidal disruption event (Brightman et al. 2021). On 2019 December 4, we detected a source in an observation of AT 2019wbg (obsID 00012842001), a candidate supernova hosted by NGC 4045. This was done with the `detect` function of the HEASOFT tool XIMAGE using a signal-to-noise threshold of 3. The X-ray source was $55''$ from AT 2019wbg and therefore not related. We used the online tool provided by the University of Leicester[8] (Evans et al. 2007, 2009) to obtain the best position of the source, which gave R.A. $= 12^{\mathrm{h}}\ 02^{\mathrm{m}}\ 42\overset{\mathrm{s}}{.}360$ ($180\overset{\circ}{.}6765$), decl. $= +1°\ 58'\ 08\overset{''}{.}54$ ($1\overset{\circ}{.}9690389$, J2000), with an uncertainty of $5\overset{''}{.}1$ (90% confidence). This placed the source outside of the nucleus of NGC 4045 and in one of its spiral arms (Figure 1). No X-ray source had been reported at this position previously. This included two Swift observations taken only 1 month prior to its initial detection as part of the Swift Gravitational Wave Galaxy Survey (Klingler et al. 2019). The position of the source had not been previously observed with Chandra, XMM-Newton, or NuSTAR.

We continued to monitor the source with already scheduled observations of AT 2019wbg and subsequent director's discretionary time (DDT) requests. We used the online tool to extract the Swift/XRT lightcurve and spectrum of NGC 4045 ULX from these observations. All products from this tool are fully calibrated and corrected for effects such as pileup and the bad columns on the CCD. The observations consisted of target IDs 12842, 33099, 89015, 03104800, 03105785, and 03105785, and the lightcurve was binned by observation, requiring a minimum detection of 2.5σ. The tool also fitted an absorbed power-law model to the stacked spectrum, which yielded the parameters $N_{\mathrm{H}} = 2.6^{+0.9}_{-0.8} \times 10^{21}\ \mathrm{cm}^{-2}$ and $\Gamma = 1.56^{+0.17}_{-0.16}$ and a count rate to unabsorbed flux conversion factor of $5.69 \times 10^{-11}\ \mathrm{erg\ cm}^{-2}\ \mathrm{ct}^{-1}$. We used this to convert the XRT count rate to flux, and assuming the distance of 32.1 Mpc to NGC 4045, convert this to a luminosity. The count rate and luminosity lightcurve is plotted in Figure 2 and shows that the source is highly variable and also regularly exceeds a luminosity of $10^{41}\ \mathrm{erg\ s}^{-1}$, classifying it as an HLX.
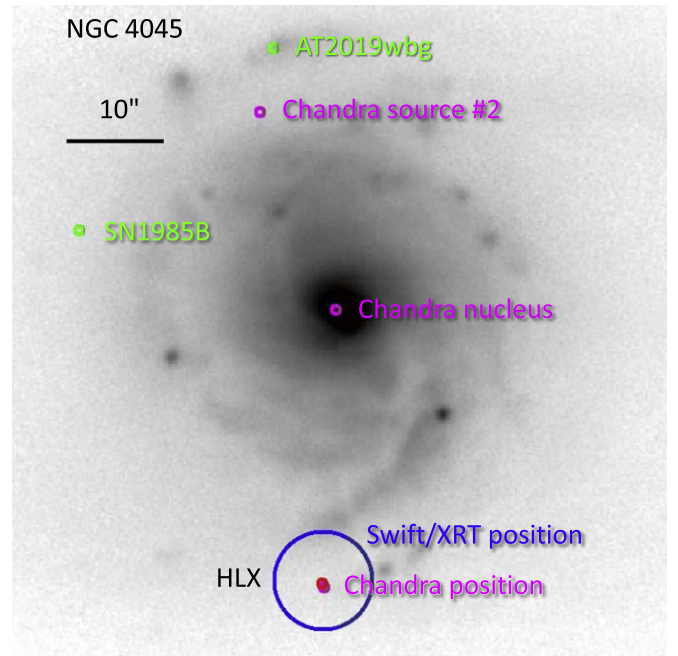
Figure 1. PanSTARRS *r*-band image of NGC 4045. The position of the X-ray source detected by Swift/XRT is shown with a blue circle where the radius represents the positional uncertainty. The more accurate position provided by Chandra is shown with a magenta circle. This appears to place the source in one of the spiral arms of the galaxy. The positions of SN 1985B and AT 2019wbg are also shown, along with the position of the nucleus and another X-ray source detected in the galaxy by Chandra.
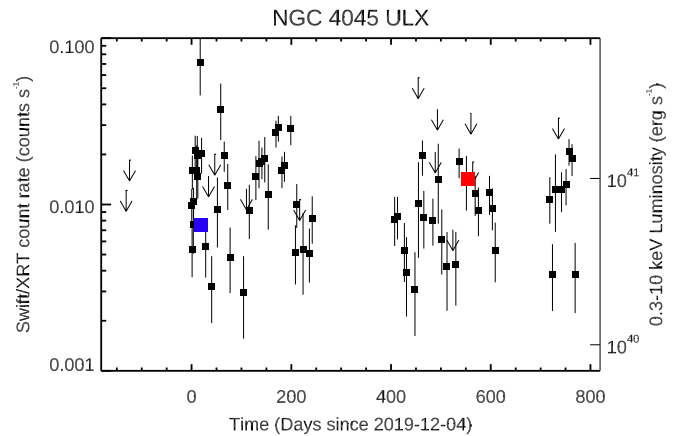

Figure 2. Swift/XRT lightcurve of the ULX in NGC 4045 (black data points). Upper limits (3σ) are shown with black arrows. The gaps in the lightcurve are due to the Swift Sun constraint. The observed 0.3–10 keV luminosity is shown on the right axis, and the luminosity of the source when observed with Chandra and NuSTAR is shown as a blue square, and when observed with XMM-Newton and NuSTAR is shown as a red square.

The hardness ratios from the online tool, defined as the ratio of the 1.5–10 keV count rate to the 0.3–1.5 keV count rate, show potential evidence for spectral evolution from the source. To investigate further, we produce spectra using the online tool for 15 observations during the period 2020 March 26 and 2020 July 19 where HR > 1, which yielded $N_{\mathrm{H}} = 3.8^{+2.2}_{-1.7} \times 10^{21}\ \mathrm{cm}^{-2}$ and $\Gamma = 1.57^{+0.32}_{-0.30}$ and a count rate to unabsorbed flux conversion factor of $6.27 \times 10^{-11}\ \mathrm{erg\ cm}^{-2}\ \mathrm{ct}^{-1}$. For the eight observations during the period 2020 December 16 and 2021 March 6 where HR < 1, $N_{\mathrm{H}} = 1.2^{+2.3}_{-1.2} \times 10^{21}\ \mathrm{cm}^{-2}$ and $\Gamma = 2.0^{+0.8}_{-0.7}$ and the count rate to unabsorbed flux conversion

factor is 4.22×10^{-11} erg cm^{-2} ct^{-1}. The N_H and Γ measured for these two epochs are consistent with each other within the 90% uncertainties; therefore, we do not find evidence for spectral variations from the Swift/XRT data.

2.2. NuSTAR

Upon identification of the new ULX, we obtained a DDT observation of the source with NuSTAR (Harrison et al. 2013). This took place on 2019 December 16 (obsID 90501355002). The source was well detected with a count rate of $5.8 \pm 0.4 \times 10^{-3}$ counts s^{-1} in FPMA and $5.1 \pm 0.4 \times 10^{-3}$ counts s^{-1} in FPMB in the 54 ks exposure over the 3–20 keV energy range. Subsequently, we obtained follow-up target of opportunity (ToO) observations of the source in NuSTAR Cycle 7. The aim was to get a longer exposure of the source at a brighter flux. This took place on 2021 June 11 (obsID 80701507002) and was triggered on the detection of a Swift/XRT count rate of >0.01 counts s^{-1} (Figure 2). The source was again well detected, this time with a higher count rate of $9.4 \pm 0.3 \times 10^{-3}$ counts s^{-1} in FPMA and $9.2 \pm 0.4 \times 10^{-3}$ counts s^{-1} in FPMB in the 100 ks exposure over the 3–20 keV energy range.

We used HEASOFT v6.28, NUSTARDAS v2.0.0, and CALDB v20211115 to analyze the data. We produced cleaned and calibrated events files using NUPIPELINE with the default settings on mode 1 data only. We used NUPRODUCTS to produce spectral data, including source and background spectra and response files. A circular region with a radius of 40″ was used to extract the source spectra. Circular regions with a radius of 90″ were used to extract the background spectra, taking care to extract the background from the same chip as the source. For timing analyses, we used the HEASOFT tool `barycorr` to apply a barycentric correction to the event times of arrival, using the default JPL planetary ephemeris DE-200.

2.3. Chandra

We also obtained a Chandra (Weisskopf 1999) DDT observation of the source, which took place on 2019 December 31 (obsID 23106), with ACIS-S at the aimpoint. The source was well detected with a count rate of $2.8 \pm 0.2 \times 10^{-2}$ counts s^{-1} in the 9.8 ks exposure. We first ran the script `chandra_repro` and then extracted the Chandra spectra with SPECEXTRACT with circular regions of radius 2″ for the source and 13″ for the background.

We also used the Chandra data to acquire a more precise position for the source. We compiled an X-ray source list of the Chandra observation by running WAVDETECT with default parameters on the reprocessed events file, filtered to energies of 0.5–8 keV. This resulted in a source list of 88 X-ray sources. We then cross-matched this with a Gaia DR3 source list of the region (Gaia Collaboration et al. 2021), selecting sources within 1″4 of each other. This identified five joint Chandra/ Gaia sources. We define the astrometric shifts as the mean difference in R.A. and decl. between these matched sources, finding δR.A. $= +0″03$ and δdecl. $= +0″79$. The Chandra position of the source, with the aforementioned corrections applied, is R.A. $= 12^h\ 02^m\ 42^s358$ ($180°67649$), decl. $= +1°$ $58'\ 07″34$ ($1°9687065$, J2000). We adopt the residual offset of $0″50$ as our uncertainty, which agrees very well with the Swift position (Figure 1). The only source at other wavelengths cataloged near this position is ULAS J120242.27+015807.6, a

UKIDSS-DR9 (Lawrence et al. 2007) $K = 17.96$ mag near-infrared source, 1″3 from the Chandra position, which is outside our positional error circle. The lack of a multi-wavelength counterpart argues against a background AGN as the source of X-rays.

We detect two other X-ray sources that are likely associated with NGC 4045. An X-ray source at R.A. $= 12^h\ 02^m\ 42^s276$, decl. $= +1°\ 58'\ 36″50$ is coincident with the Gaia position of the nucleus of the galaxy, 29″ from the ULX. It has a count rate of $1.9 \pm 0.4 \times 10^{-3}$ counts s^{-1}, corresponding to a flux of 3×10^{-14} erg cm^{-2} s^{-1} in the 0.5–8 keV band, implying a luminosity of 4×10^{39} erg s^{-1} at 32 Mpc. This source is likely to be the AGN of NGC 4045, which is at low luminosity.

The other source was at R.A. $= 12^h\ 02^m\ 42^s799$, decl. $= +1°$ $58'\ 56″98$ in the northern spiral arm of the galaxy, 50″ from the ULX, and close to, but not coincident with AT 2019wbg (Figure 1). It has a count rate of $2.0 \pm 1.4 \times 10^{-4}$ counts s^{-1}, corresponding to a flux of 1.7×10^{-14} erg cm^{-2} s^{-1} in the 0.3–10 keV band, implying a luminosity of 2×10^{39} erg s^{-1} at 32 Mpc and therefore also a ULX.

2.4. XMM-Newton

In our NuSTAR Cycle 7 program, we were awarded joint observations with XMM-Newton (Jansen et al. 2001). XMM-Newton observed NGC 4045 on 2021 June 12 (obsID 0890610101). We used XMMSAS v18.0.0 to analyze the data (Gabriel et al. 2004). We first checked for high background by creating a lightcurve of the events from the entire detector in the 10–12 keV band, finding that the background was low across the entire observation, with less than 0.7 counts s^{-1} in this band for the pn detector and less than 0.35 counts s^{-1} in the MOS detectors. Events were selected with PATTERN $\leqslant 4$ for the pn and PATTERN $\leqslant 12$ for the MOS. A circular region with a radius of 20″ was used to extract the source spectrum. A circular region with a radius of 45″ was used to extract the background spectra. Care was taken to extract the background from the same chip as the source and from the region of low internal detector Cu Kα fluorescence background, located at the center of the detector near where the source was placed (Freyberg et al. 2004). Data from the pn and both MOS instruments were extracted in this way. For timing analyses, we used the XMMSAS tool `barycen` to apply a barycentric correction to the event times of arrival using the default DE-200 solar ephemeris

The source was well detected with a count rate of $1.57 \pm 0.01 \times 10^{-1}$ counts s^{-1} in pn, $5.06 \pm 0.09 \times 10^{-2}$ counts s^{-1} in MOS1, and $5.2 \pm 0.10 \times 10^{-2}$ counts s^{-1} in MOS2 in the 61 ks exposure over the 0.2–10 keV energy range.

3. X-Ray Spectral Analysis

We summarize the details of all NuSTAR, Chandra, and XMM-Newton observations of the new HLX in Table 1. All spectra were grouped with a minimum of one count per bin using the HEASOFT tool `grppha` and fitted in XSPEC (Arnaud 1996). The C statistic was used for fitting to source spectra with the background subtracted (Cash 1979). Because the C statistic cannot formally be used when the background is subtracted, XSPEC uses a modified version of the C statistic, known as the W statistic, to account for this. The data are shown in Figure 3, top panel.

Table 1
Details of the Observations Used in This Work

Observatory	ObsID	Start Time (UT)	Instrument	Exposure[a] (ks)	Net Count Rate (counts s^{-1})	Flux[b] (erg cm^{-2} s^{-1})
NuSTAR	90501355002	2019-12-16 02:01:09	FPMA	53.9	$5.8 \pm 0.4 \times 10^{-3}$	$4.4^{+0.3}_{-1.0} \times 10^{-13}$
			FPMB	53.4	$5.1 \pm 0.4 \times 10^{-3}$	$3.9^{+0.3}_{-1.1} \times 10^{-13}$
Chandra	23106	2019-12-31 05:56:24	ACIS-S	9.8	$2.8 \pm 0.2 \times 10^{-2}$	$3.9^{+0.3}_{-1.0} \times 10^{-13}$
NuSTAR	80701507002	2021-06-11 18:51:09	FPMA	101	$9.4 \pm 0.3 \times 10^{-3}$	$7.2^{+0.3}_{-1.0} \times 10^{-13}$
			FPMB	99.6	$9.2 \pm 0.4 \times 10^{-3}$	$7.3^{+0.3}_{-1.4} \times 10^{-13}$
XMM-Newton	0890610101	2021-06-12 04:11:07	pn	53.1	$1.6 \pm 0.2 \times 10^{-1}$	$8.1^{+0.0}_{-2.0} \times 10^{-13}$
			MOS1	50.6	$5.1 \pm 0.9 \times 10^{-2}$	$8.1^{+0.2}_{-1.9} \times 10^{-13}$
			MOS2	61.4	$5.2 \pm 1.0 \times 10^{-2}$	$7.9^{+0.0}_{-1.9} \times 10^{-13}$

Notes.
[a] After filtering.
[b] 0.5–8 keV for Chandra, 0.2–10 keV for XMM-Newton, and 3–20 keV for NuSTAR, observed (absorbed).

3.1. Continuum Fitting

We fit the Chandra, XMM-Newton, and NuSTAR observations of the source jointly in XSPEC with the use of a `constant` component to account for the flux variability of the source and cross-calibration offsets. We start by fitting a simple absorbed power-law model, `tbabs*powerlaw`, with the abundances of Anders & Grevesse (1989), which yields $C = 4287.24$ with 4694 degrees of freedom (DoFs). However, the data to model residuals reveal a spectral turnover, with an energy of $6.7^{+1.1}_{-0.9}$ keV when fitting with the `cutoffpl` model, indicating that this simple model does not represent the data well. Replacing the power-law model with a multicolor disk blackbody model, with a variable temperature profile index (`diskpbb`), improves the fit substantially to $C = 4121.29$ with 4693 DoFs. While this model appears to represent the data well, ULX spectra often exhibit two disk-like components, a cooler one, which may come from the outer regions of an accretion disk or the photosphere of an outflow (Qiu & Feng 2021), and a hotter component, which may originate from the inner regions of the accretion disk (Walton et al. 2018b), an accretion curtain (Mushtukov et al. 2017), or Compton upscattering (Gladstone et al. 2009). We therefore tried the addition of a second cooler disk-like component, `diskbb`, which gives $C = 4117.17$ with 4691 DoFs, only a minor improvement to the fit. This is probably due to the relatively high absorption in the system and the dominance of the hotter component. However, we keep it for comparison to other ULXs. The fit with this model is shown in Figure 3, middle panel, and we list the spectral parameters and their uncertainties in Table 2.

We tested for spectral variability between the 2019 Chandra+NuSTAR observations and the 2021 XMM-Newton+NuSTAR observations by allowing the parameters to vary in the fit one by one and calculating their 90% uncertainties. We found no evidence for spectral variability, finding that the parameters were consistent with each other within the 90% confidence uncertainties between epochs.

3.2. Absorption-line Fitting

While the spectral residuals do not indicate any other continuum model components, we noted a deficit of counts in the 8–9 keV band that could be an absorption line (Figure 4). To test this hypothesis, we add a Gaussian absorption component `Gauss` to the fit. This yields $C = 4099.62$ with

4688 DoFs, an improvement to the fit of $\Delta C = -17.5$ with the loss of 3 DoFs. The contributions to the observed change in C are $\Delta C = -3.7$ from FPMA+B (2019), $\Delta C = -6.9$ from FPMA+B (2021), $\Delta C = -6.2$ from pn, and -0.5 from MOSs. This shows that the improvement in the fit is not driven by a single instrument, or observing epoch, indicating that the absorption feature is neither instrumental nor transient.

We first determine the false-alarm rate (FAR), the probability that a change in C with this magnitude is a statistical fluctuation. We do this with simulations using the `fakeit` command in XSPEC. We generate 6000 simulated spectra from each instrument based on the continuum `tbabs*(diskbb +diskpbb)` model only and the observed background and instrumental responses. We generate unbinned data from these and group them with a minimum of one count per bin as done with the real data.

We then refit the simulated spectra with the continuum model and add the `Gauss` component. Because we cannot visually search each simulated spectrum for residuals as done for the real data, in order to ensure we find the strongest residual in each simulated spectrum, we perform a Gaussian line scan using the `steppar` command in XSPEC to search over the line energy in the 2–10 keV energy range in 80 equally and linearly spaced steps. This procedure fits the spectrum at each step, with the line energy and width fixed but the normalization free to vary. The line width is fixed at 0.1 keV to simulate the unresolved nature of the real feature. For each simulated spectrum set, we note the largest change in C when carrying out the line search. We plot the distribution of these maximum C values in Figure 5. Only seven simulated spectrum sets produce a ΔC as large as that observed, implying an FAR of 1.2×10^{-3}.

Because the number of simulated ΔC is very small at large negative values, this FAR is subject to small number statistics. We also plot the cumulative ΔC distribution in Figure 5, which is basically the FAR for a given ΔC when normalized by the number of simulations. The ΔC and cumulative ΔC distributions clearly take a power-law form for $\Delta C > -15$, below which small number statistics skew the distributions. We then fit the ΔC distribution analytically for $\Delta C > -15$ and extrapolate to more negative values to determine the precise FAR. Fitting the cumulative ΔC distribution with a power-law yields a power-law index of 0.090. This predicts the number of simulations where $\Delta C < -17.5$ is 5.1, which when divided by 6000 implies the FAR is 8.5×10^{-4}. This is equivalent to
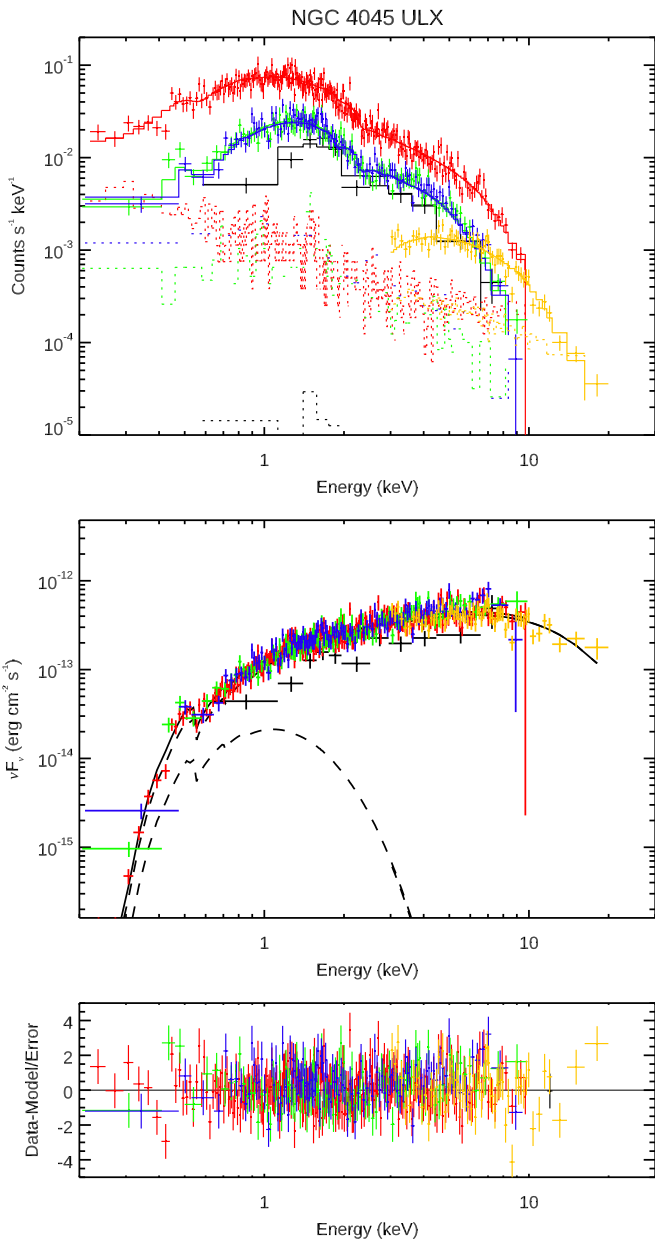
Figure 3. Chandra (black), XMM-Newton/pn (red), XMM-Newton/MOS1 (green), XMM-Newton/MOS2 (blue), and NuSTAR (both epochs FPMA+B, stacked, yellow) spectra of the ULX in NGC 4045. The top panel shows the data with best-fit `tbabs*(diskbb+diskpbb)` model (solid line) and background for each instrument (dotted lines), the middle panel shows the data unfolded through the instrumental responses when assuming the best-fit model, and the bottom panel shows the spectral residuals, rebinned for plotting purposes.

$> 3.3\sigma$, which confirms that the absorption line is significantly detected. The implied 3σ ΔC threshold is -15.2.

The best-fit parameters of the Gaussian absorption line for all instruments together are a line energy $E = 8.56^{+0.05}_{-0.11}$ keV, width $\sigma < 0.2$ keV, and normalization $K = -7.4^{+2.6}_{-2.4} \times 10^{-7}$ photons cm^{-2} s^{-1} with an equivalent width EW $= -0.22^{+0.08}_{-0.09}$ keV. We also tested for spectral variability of the absorption line between observational epochs but found no evidence for it. We show the contour plot of the energy and width of the line in Figure 6, showing that the width of the line is unconstrained at

Table 2
Joint X-Ray Continuum Spectral Fitting Results

	`tbabs`
$N_{\rm H}$	$2.1^{+0.9}_{-0.4} \times 10^{21}$ cm^{-2}
	`diskbb`
$T_{\rm in}$	$0.27^{+0.19}_{-0.08}$ keV
Normalization	$0.74^{+11}_{-0.71}$
	`diskpbb`
$T_{\rm in}$	$3.27^{+0.38}_{-0.32}$ keV
p	$0.60^{+0.04}_{-0.03}$
Normalization	$2.0^{+1.7}_{-0.9} \times 10^{-4}$
	`constant`
$C_{\rm FPMA,2019}$	0.67 ± 0.07
$C_{\rm FPMB,2019}$	$0.60^{+0.07}_{-0.08}$
$C_{\rm ACIS}$	$0.56^{+0.06}_{-0.05}$
$C_{\rm FPMA,2021}$	1.08 ± 0.07
$C_{\rm FPMB,2021}$	$1.09^{+0.07}_{-0.08}$
$C_{\rm pn}$	1.00 (fixed)
$C_{\rm MOS1}$	1.01 ± 0.04
$C_{\rm MOS2}$	0.98 ± 0.04
$F_{\rm X}$ (0.2–20 keV)[a]	$9.8^{+0.1}_{-1.9} \times 10^{-13}$ erg cm^{-2} s^{-1}
$L_{\rm X}$(0.001–100 keV)[b]	$1.5^{+0.6}_{-0.1} \times 10^{41}$ erg s^{-1}
C statistic	4117.17
DoFs	4691

Notes. Results from the continuum spectral fitting of the NuSTAR, Chandra, and XMM-Newton data.
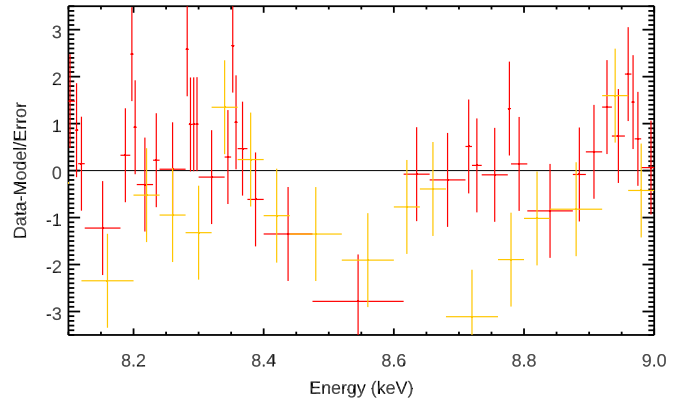[a] Observed.
[b] Unabsorbed.

Figure 4. Spectral residuals of the best-fit continuum model in the 8–9 keV band, where a deficit of counts can be seen at ∼8.5 keV. XMM-Newton/pn (red) and NuSTAR (both epochs FPMA+B, stacked, yellow) are plotted, rebinned for plotting purposes. Chandra and MOS data are omitted for clarity.

the lower end due to it being close to the instrumental energy resolution of XMM-Newton/pn. This also shows the constraints provided by the pn, and two FPMA epochs showing they are all consistent with each other within their 1σ confidence levels.

We also test the possibility that the 8.56 keV feature is an absorption edge rather than a line doing so using the `edge` model in XSPEC. Adding this parameter to the continuum model yields $C = 4107.98$ with 4689 DoFs, an improvement over the fit of $\Delta C = -9.2$, with the loss of 2 DoFs. This is not as great an improvement as the line case, despite one fewer DoF; therefore, we conclude that the feature is more line like than edge like.
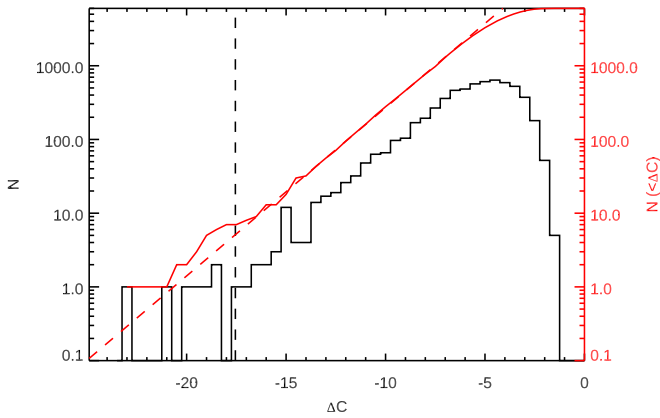
Figure 5. Results of the 5000 spectral simulations used to determine the significance of the absorption line at 8.58 keV. The black histogram shows the distribution of ΔC produced by the simulations, and the dashed black line shows the observed value. Only six simulated values exceed the ΔC observed. The solid red line shows the cumulative distribution of the ΔC produced by the simulations, and the red dashed line is a fit to this distribution, which implies the number of simulated spectra that produce a ΔC as large as that observed is 5.1.
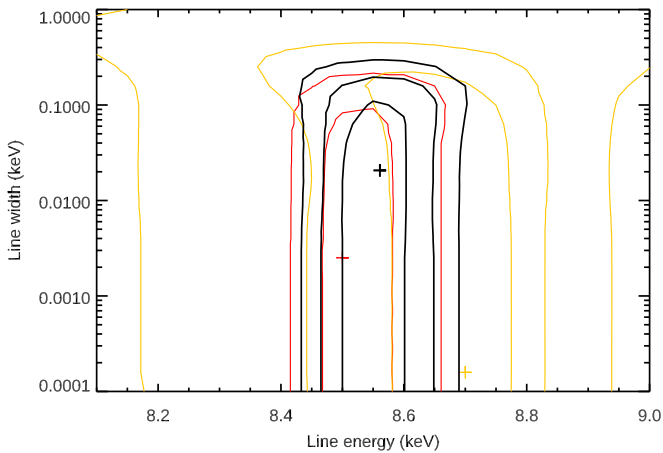
Figure 6. 1σ, 2σ, and 3σ C-statistic contours of the energy and width of the Gaussian absorption line for all instruments together (black), for XMM-Newton/pn (red), and for NuSTAR/FPMA+B (yellow, 2019 and 2021 epochs) when fitted individually.

3.3. Potential Identification as Absorption by a Highly Ionized Outflow

The 8.56 keV absorption line is potentially associated with a highly ionized outflow produced by a high-velocity disk wind. In an attempt to understand the properties of the potential ionized outflow, we fit the NuSTAR and XMM-Newton spectra with the PION spectral model within the SPEX package (Kaastra et al. 1996). PION (e.g., Miller et al. 2015) determines the ionizing balance and the absorption-line strengths from the spectral energy distribution of the currently loaded SPEX continuum model. If the data quality is sufficient, the model might allow us to measure the ionization parameter (ξ), column density ($N_{\rm H}$), as well as the projected velocity (v) of the outflow. Then it would be possible to estimate the outflow energetics.

Because PION is based in SPEX, the continuum models used here are slightly different from those used above in XSPEC. The hotter spectral component is modeled with an MBB component (a blackbody modified by coherent Compton scattering), with a temperature of ~ 3 keV. The cooler spectral component is

modeled by a simple blackbody with a temperature of 0.3–0.4 keV. Both are obscured by the HOT component, which describes the transmission through a layer of collisionally ionized plasma, with a temperature of 0.5 eV, simulating nearly neutral ISM plasma in collisional equilibrium, and assumes the abundances of Lodders et al. (2009). The column density is $N_{\rm H} \sim 8 \times 10^{20}$ cm^{-2} and describes the interstellar absorption in both our Galaxy and NGC 4045. We do not find evidence for any additional continuum components.

This continuum model is used to fit all the XMM-Newton and NuSTAR spectra, converted to the SPEX file format using the Trafo procedure, in the appropriate energy ranges, binned to at least one count per spectral bin. The component parameters including normalizations are tied across the observations, with only the overall model normalization being left free to vary. The resulting continuum model results in $C = 4157.69$ with 4736 DoF.

Following the continuum fit, we applied the PION model. The fit statistics improved to $C = 4141.83$ with the loss of four DoFs, for a fit improvement of $\Delta C = -15.86$. We find a column density $N_{\rm H} = 2^{+0.0}_{-0.7} \times 10^{24}$ cm^{-2}, an ionization parameter $\log(\xi/{\rm erg\,cm\,s}^{-1}) = 4.70 \pm 0.14$, a velocity width of 2900^{+2200}_{-1200} km s^{-1}, and a projected systematic velocity of $61{,}200^{+1700}_{-1500}$ km s^{-1} (relativistically corrected). Unfortunately, the column density of the PION model is pegged to our upper limit of 2×10^{24} cm^{-2}. This is a very high value, exceeding the ultrafast outflow (UFO) column densities measured in both ULXs and AGNs (e.g., Tombesi et al. 2011; Pinto et al. 2016, 2021). An outflow of such high column density would plausibly produce a strong associated emission signature such as a P Cygni feature with a strong emission component, but this is not observed in the current spectra. However, the presence of a P Cygni profile depends on the exact geometry and solid angle of the wind responsible for the Fe K feature. Additionally, such a high column density requires a very large unabsorbed 0.3–30 keV X-ray luminosity of 7×10^{41} erg s^{-1}, higher than that observed and on the very upper end of the ULX luminosity function.

Therefore, we do not consider such a high $N_{\rm H}$ value to be trustworthy. The poor data quality could be the reason for the unrealistic value. At such high-ionization levels, the ionization parameter and thus the column density are determined from the ratio of the Fe XXV (rest-frame energy of 6.67 keV) and Fe XXVI (6.97 keV) absorption-line strengths. The poor data quality could result in a very inaccurate measurement of this ratio. Additionally, by increasing the column density (and thus the ionization parameter), the PION model increases the absorption strengths of the Fe K lines while decreasing the strengths of the lower energy lines such as O VIII, Ne X, Si XIV, and S XVI. These lower energies (<3 keV) are poorly resolved with the EPIC detectors (and outside the NuSTAR range) but it appears that no (even weak) absorption residuals are present at the appropriate energies of the other elements. Thus, PION chooses to reduce the line strengths as much as possible. Naturally, no additional (lower energy) absorption features would be expected in case the residual is due to noise or is a cyclotron resonance feature, but this could still be a spectral resolution issue (at the present data quality) in the soft X-ray band. The column density could also be reduced by increasing the Fe abundance; however, the abundance value is highly degenerate with the absorber column density, and we could not obtain a reasonable fit.

Further, longer XMM-Newton and NuSTAR observations of the source might improve the data quality, leading to a more confident UFO parameter measurement, allowing us to estimate the wind energetics. An RGS grating detection of the blueshifted O VIII feature (expected around 0.8 keV) would lead to a much more trustworthy plasma parameter measurement.

The column density is strongly degenerate with the ionization parameter. We can therefore fix $\log \xi$ to a more realistic value and recover the column density. Assuming $\log(\xi/\mathrm{erg\,cm\,s}^{-1}) = 3.92$, the best-fitting ionization parameter of the UFO in the neutron star ULX NGC 300 ULX-1 (Kosec et al. 2018b), we recover a column density of $2.2^{+0.9}_{-0.7} \times 10^{23}$ cm^{-2}. This is a much more realistic N_H value, comparable with the one measured in NGC 300 ULX-1 (best-fitting column density of $1.2^{+1.9}_{-0.6} \times 10^{23}$ cm^{-2}). However, the addition of a PION component of such parameters results in a poorer fit improvement of just $\Delta C = -13.7$ over the baseline continuum model.

3.4. Potential Identification as a Cyclotron Resonance Scattering Feature

Above we explored the identification of the 8.56 keV absorption line with absorption by highly ionized iron. Here we explore the possibility that the absorption line is a CRSF, produced by the interaction of X-ray photons with a strong magnetic field. This would naturally identify the compact object as a neutron star because black holes are not capable of producing such strong magnetic fields.

To test this possibility, we trial the use of the XSPEC model `cyclabs` (Makishima et al. 1990; Mihara et al. 1990). This model utilizes two Lorentzian functions to represent the fundamental and first harmonic lines, with the energy of the harmonic fixed at twice the energy of the fundamental. We assume the 8.56 keV line to be the fundamental and set the width of the harmonic line to be the same as the fundamental. Adding and fitting this model to our continuum model yields $C = 4101.73$ with 4687 DoFs, slightly worse than the single-Gaussian absorption line.

The energy of the fundamental is $E = 8.56^{+0.09}_{-0.08}$ keV with a width of $W < 0.12$ keV and an optical depth of $1 \leqslant D_0 \leqslant 6 \times 10^3$. The energy of the harmonic is implied to be 17.1 keV; however, the depth is unconstrained with an upper limit of $D_2 \leqslant 6 \times 10^4$. This loose constraint is because the number of counts and signal to noise of the NuSTAR data at this energy are low. Determining the presence of a harmonic line is key to identifying the line as a CRSF, especially when the fundamental line has an energy consistent with atomic absorption. However, we are unable to do this with the current data.

Alternatively, if we assume the 8.6 keV line is the harmonic and the fundamental is at 4.3 keV, then we can place an upper limit of 180 on the depth of the fundamental, compared with a lower limit of 660 on the harmonic, i.e., the depth of the harmonic is constrained to be >3 times that of the fundamental.

3.5. Potential AGN Contamination

As described in Section 2.3, we identified a low-luminosity AGN in NGC 4045 in the Chandra data. The AGN was 29″ from the ULX, and therefore potentially contaminates the XMM-Newton and NuSTAR PSFs of the source. We extracted the Chandra spectrum of the AGN and fitted it with an absorbed power law, which yielded $N_\mathrm{H} < 3 \times 10^{21}$ cm^{-2} and $\Gamma = 2.9^{+1.2}_{-0.9}$ with a 0.5–8 keV flux of 3×10^{-14} erg cm^{-2} s^{-1}, less than 10% of the flux of the ULX. The spectrum is also softer than the ULX, contributing less than 1% of the flux in the 8–9 keV band where the absorption line was identified. We therefore rule out AGN contamination as a source of error in the absorption-line analysis.

4. Pulsation Search

We searched for pulsations in the XMM-Newton and NuSTAR data using the `HENDRICS` command-line tools, which are based on the `Stingray` package (Bachetti 2018; Huppenkothen et al. 2019). In particular, we used `HENaccelsearch` to search for pulsations between 0.006 and 2 Hz (0.5–167 s), a range in which most ULX pulsars are found. We could not find any significant pulsations, either in XMM-Newton or in the NuSTAR data in this range, likely due to too few counts collected.

We then proceeded to calculate upper limits on the pulsed fraction of any possible pulsation between 0.1 and 1 Hz. To do that, we simulated event files through a Poisson process with the same number of events, exposure time, and GTI windows, but injected a sinusoidal pulsation profile with a given pulsed fraction. For each pulsed fraction, we performed 60 simulations and measured how often we could recover the pulsations at the 99% significance limit and determine the upper limit on the pulsed fraction (PF) to be where this is the case for 90% of all simulations. Based on these simulations, we find PF < 15% for XMM-Newton and PF < 35% for NuSTAR. The PF for ULX pulsars is ∼10%–30%, increasing with energy (e.g., Bachetti et al. 2014; Fürst et al. 2016; Israel et al. 2017b).

5. Discussion

5.1. The Broadband X-Ray Spectrum of NGC 4045 ULX

The current sample of ULXs with high-quality broadband X-ray spectra is relatively small, only ∼10 sources (Walton et al. 2018b). We can now add NGC 4045 ULX to that sample. The broadband X-ray spectrum of NGC 4045 ULX can be well described by two disk-like components similar to other ULXs (Middleton et al. 2015; Koliopanos et al. 2017; Pintore et al. 2017; Walton et al. 2018b). One of these is potentially associated with the hot, large-scale-height inner flow, and the other is a cooler component, perhaps associated with the outer part of the disk or the photosphere of an outflow. Furthermore, a high-energy tail is often detected, possibly associated with the accretion column of a pulsar, or Comptonized emission. As presented by Walton et al. (2018b), this component, which can be modeled with a `cutoffpl` model, can often be seen as well. If we add this model to our fit, with $\Gamma = 0.5$ and $E_\mathrm{cut} = 8.1$ keV fixed, the fit improves slightly to $C = 4112.93$ with 4690 DoFs. In the sample of Walton et al. (2018b) fitted with the three-component model, the temperature of the cool component for ULXs ranges from 0.2 to 0.5 keV and the hotter component has a temperature range of 1.2–3 keV. We find for NGC 4045 ULX that the cool disk-like component has a temperature of 0.40 keV, while the hot one has a temperature of 2.1 keV for NGC 4045 ULX, completely consistent with other ULXs. Walton et al. (2018b) also noted that the ratio of the temperatures of these two components for ULX pulsars in their sample was ∼3, while the other ULXs had a temperature ratio

of ∼8. For the NGC 4045 ULX, the ratio is 5, in between the wider ULX population and ULX pulsars.

5.2. An Ultrafast Outflow from NGC 4045 ULX

If the 8.56 keV absorption line is from highly ionized iron, it is either from Fe XXV with a rest-frame energy of 6.67 keV or from Fe XXVI with a rest-frame energy of 6.98 keV, making the outflow velocity in our line of sight $v = 0.23$–$0.28c$, similar to the velocities of the outflows seen in other ULXs (0.1–0.3c, e.g., Pinto et al. 2016). Unfortunately, we could not model the parameters of the outflow well from this single line. The EW is high, $-0.22^{+0.08}_{-0.09}$ keV, several times stronger than the UFO seen in the Fe K band for NGC 1313 X-1 (-61 eV, Walton et al. 2016), and requires a high-ionization state, column density, or both.

5.3. A Neutron Star Powering NGC 4045 ULX?

If the 8.56 keV absorption line is produced by cyclotron resonance scattering of X-ray photons by charged particles in the presence of a powerful magnetic field, this would imply that NGC 4045 ULX is powered by a neutron star because black holes cannot produce such strong magnetic fields. If the charged particles are electrons, the transition energy, ΔE, is $11.6(1 + z)^{-1}(B/10^{12}$ G) keV, where $z = (1 - 2GM/r_{cyc}c^2)^{-1/2} - 1$ (r_{cyc} is the radius at which the CRSF forms, assumed to be the surface of the neutron star) is the gravitational redshift and is ∼0.25 for the emission from the surface of a typical neutron star. The 8.56 keV line that we have detected would therefore imply $B = 7(1 + z) \times 10^{11}$ G. If the charged particles are protons, $\Delta E = 6.3(1 + z)^{-1}(B/10^{15}$ G) keV; thus, interpreting our observed line as a proton CRSF would imply a very high magnetic field strength of $1.4(1 + z) \times 10^{15}$ G.

For Galactic pulsars with known electron CRSFs, the features are typically broad with Gaussian line widths of order ∼1 keV and are seen mostly at energies above 10 keV, giving broadening ratios $\sigma/E \sim 0.1$ (Tsygankov et al. 2006; Jaisawal & Naik 2016). Protons, on the other hand, are more massive and should produce narrower lines. The few proton CRSFs observed to date were indeed narrow ($\sigma < 0.4$ keV) and at energies below 10 keV (Ibrahim et al. 2002), giving broadening ratios of $\sigma/E < 0.1$. The broadening ratio of the line we have observed is <0.014 and therefore more comparable to the previously reported proton CRSFs. However, NGC 4045 ULX is the most luminous source with a potential CRSF identified so far, so drawing a connection to lower-luminosity neutron star systems may be tenuous.

The detection of a harmonic line would be key in confirming the CRSF scenario and for identifying the charged particles as electrons or protons. In Galactic pulsars, the fundamental line is often observed to be weaker than the harmonic line due to photon spawning, caused by transitions from high to low Landau levels that produce photons at the energy of the fundamental line (Araya & Harding 1999). This effect is strongest for electrons and for hard X-ray spectra. The harmonic line is expected at 17 keV and thus only currently observable with NuSTAR.

Finally, while no pulsations have yet been detected from NGC 4045 ULX, which would also unambiguously identify a neutron star powering it, we cannot rule out pulsations because the upper limits on the pulsed fraction we derive are above those of the typical ULX pulsar.

5.4. Summary and Conclusions

We have identified a new HLX ($L_X > 10^{41}$ erg s^{-1}) in the galaxy NGC 4045 at a distance of 32 Mpc. We have presented Swift, NuSTAR, Chandra, and XMM-Newton observations of the source that show the broadband spectrum being very similar to other ULXs. We have also found an absorption line significantly detected ($>3.3\sigma$) at 8.56 keV, which appears most likely to be the signature of a highly ionized ultrafast outflow. However, the large EW of the line (EW $= -0.22^{+0.08}_{-0.09}$ keV) paired with the lack of other absorption lines detected requires a high column density and ionization parameter, in which case a P Cygni line profile would be expected, combined with a high luminosity. An alternative explanation is that the line is due to a CRSF, produced by the interaction of X-ray photons with a powerful magnetic field. Further observations with high spectral resolution at low energies to detect other signatures of the outflow or deeper observations at >10 keV to detect the harmonic line of the CRSF are needed to differentiate between these scenarios.

ORCID iDs

Murray Brightman ⬤ https://orcid.org/0000-0002-8147-2602
Felix Fürst ⬤ https://orcid.org/0000-0003-0388-0560
Hannah Earnshaw ⬤ https://orcid.org/0000-0001-5857-5622
Marianne Heida ⬤ https://orcid.org/0000-0002-1082-7496
Matthew J Middleton ⬤ https://orcid.org/0000-0002-8183-2970
Daniel Stern ⬤ https://orcid.org/0000-0003-2686-9241
Dominic J Walton ⬤ https://orcid.org/0000-0001-5819-3552

References

Anders, E., & Grevesse, N. 1989, GeCoA, 53, 197
Araya, R. A., & Harding, A. K. 1999, ApJ, 517, 334
Arnaud, K. A. 1996, in ASP Conf. Ser. 101, Astronomical Data Analysis Software and Systems V, ed. G. H. Jacoby & J. Barnes (San Francisco, CA: ASP), 17
Bachetti, M. 2015, MaLTPyNT: Quick Look Timing Analysis for NuSTAR Data, Astrophysics Source Code Library, ascl:1502.021
Bachetti, M. 2018, HENDRICS: High ENergy Data Reduction Interface from the Command Shell, Astrophysics Source Code Library, ascl:1805.019
Bachetti, M., Harrison, F. A., Walton, D. J., et al. 2014, Natur, 514, 202
Brightman, M., Harrison, F. A., Fürst, F., et al. 2018, NatAs, 2, 312
Brightman, M., Ward, C., Stern, D., et al. 2021, ApJ, 909, 102
Burrows, D. N., Hill, J. E., Nousek, J. A., et al. 2005, SSRv, 120, 165
Carpano, S., Haberl, F., Maitra, C., & Vasilopoulos, G. 2018, MNRAS, 476, L45
Cash, W. 1979, ApJ, 228, 939
Evans, P. A., Beardmore, A. P., Page, K. L., et al. 2007, A&A, 469, 379
Evans, P. A., Beardmore, A. P., Page, K. L., et al. 2009, MNRAS, 397, 1177
Farrell, S. A., Webb, N. A., Barret, D., Godet, O., & Rodrigues, J. M. 2009, Natur, 460, 73
Freyberg, M. J., Briel, U. G., Dennerl, K., et al. 2004, Proc. SPIE, 5165, 112
Fürst, F., Walton, D. J., Harrison, F. A., et al. 2016, ApJL, 831, L14
Fürst, F., Walton, D. J., Stern, D., et al. 2017, ApJ, 834, 77
Gabriel, C., Denby, M., Fyfe, D. J., et al. 2004, in ASP Conf. Ser. 314, Astronomical Data Analysis Software and Systems (ADASS) XIII, ed. F. Ochsenbein, M. G. Allen, & D. Egret (San Francisco, CA: ASP), 759
Gaia Collaboration, Brown, A. G. A., Vallenari, A., et al. 2021, A&A, 649, A1
Gavazzi, G., Savorgnan, G., & Fumagalli, M. 2011, A&A, 534, A31
Gehrels, N., Chincarini, G., Giommi, P., et al. 2004, ApJ, 611, 1005
Gladstone, J. C., Roberts, T. P., & Done, C. 2009, MNRAS, 397, 1836
Gnedin, I. N., & Sunyaev, R. A. 1974, A&A, 36, 379
Harrison, F. A., Craig, W. W., Christensen, F. E., Hailey, C. J., & Zhang, W. W. 2013, ApJ, 770, 103
Huppenkothen, D., Bachetti, M., Stevens, A. L., et al. 2019, ApJ, 881, 39
Ibrahim, A. I., Safi-Harb, S., Swank, J. H., et al. 2002, ApJL, 574, L51
Israel, G. L., Belfiore, A., Stella, L., et al. 2017a, Sci, 355, 817
Israel, G. L., Papitto, A., Esposito, P., et al. 2017b, MNRAS, 466, L48
Jaisawal, G. K., & Naik, S. 2016, MNRAS, 461, L97
Jansen, F., Lumb, D., Altieri, B., et al. 2001, A&A, 365, L1
Kaastra, J. S., Mewe, R., & Nieuwenhuijzen, H. 1996, in UV and X-ray Spectroscopy of Astrophysical and Laboratory Plasmas, 411
Klingler, N. J., Kennea, J. A., Evans, P. A., et al. 2019, ApJS, 245, 15
Koliopanos, F., Vasilopoulos, G., Godet, O., et al. 2017, A&A, 608, A47
Kosai, H., Kozai, Y., & Horiguchi, S. 1985, IAUC, 4035, 1
Kosec, P., Pinto, C., Fabian, A. C., & Walton, D. J. 2018a, MNRAS, 473, 5680
Kosec, P., Pinto, C., Walton, D. J., et al. 2018b, MNRAS, 479, 3978
Lawrence, A., Warren, S. J., Almaini, O., et al. 2007, MNRAS, 379, 1599
Lodders, K., Palme, H., & Gail, H. P. 2009, LanB, 4B, 712
Makishima, K., Mihara, T., Ishida, M., et al. 1990, ApJL, 365, L59
Middleton, M. J., Heil, L., Pintore, F., Walton, D. J., & Roberts, T. P. 2015, MNRAS, 447, 3243
Middleton, M. J., Walton, D. J., Roberts, T. P., & Heil, L. 2014, MNRAS, 438, L51
Mihara, T., Makishima, K., Ohashi, T., Sakao, T., & Tashiro, M. 1990, Natur, 346, 250
Miller, J. M., Kaastra, J. S., Miller, M. C., et al. 2015, Natur, 526, 542
Mushtukov, A. A., Suleimanov, V. F., Tsygankov, S. S., & Ingram, A. 2017, MNRAS, 467, 1202
Pinto, C., Alston, W., Soria, R., et al. 2017, MNRAS, 468, 2865
Pinto, C., Middleton, M. J., & Fabian, A. C. 2016, Natur, 533, 64
Pinto, C., Soria, R., Walton, D. J., et al. 2021, MNRAS, 505, 5058
Pinto, C., Walton, D. J., Kara, E., et al. 2020, MNRAS, 492, 4646
Pintore, F., Zampieri, L., Stella, L., et al. 2017, ApJ, 836, 113
Poutanen, J., Lipunova, G., Fabrika, S., Butkevich, A. G., & Abolmasov, P. 2007, MNRAS, 377, 1187
Qiu, Y., & Feng, H. 2021, ApJ, 906, 36
Rodríguez Castillo, G. A., Israel, G. L., Belfiore, A., et al. 2020, ApJ, 895, 60
Sathyaprakash, R., Roberts, T. P., Walton, D. J., et al. 2019, MNRAS, 488, L35
Shakura, N. I., & Sunyaev, R. A. 1973, A&A, 24, 337
Tombesi, F., Cappi, M., Reeves, J. N., et al. 2011, ApJ, 742, 44
Truemper, J., Pietsch, W., Reppin, C., et al. 1978, ApJL, 219, L105
Tsygankov, S. S., Lutovinov, A. A., Churazov, E. M., & Sunyaev, R. A. 2006, MNRAS, 371, 19
Tully, R. B., Courtois, H. M., & Sorce, J. G. 2016, AJ, 152, 50
Walton, D. J., Bachetti, M., Fürst, F., et al. 2018a, ApJL, 857, L3
Walton, D. J., Fürst, F., Heida, M., et al. 2018b, ApJ, 856, 128
Walton, D. J., Mackenzie, A. D. A., Gully, H., et al. 2022, MNRAS, 509, 1587
Walton, D. J., Middleton, M. J., Pinto, C., et al. 2016, ApJL, 826, L26
Weisskopf, M. C. 1999, arXiv:astro-ph/9912097